Sensors and Materials, Vol. 37, No. 9 (2025) 4285–4295
MYU Tokyo

S & M 4181

Design and Fabrication of a High-efficiency Light Absorber for Visible-spectrum Photodetectors

Chia-Te Liao,[1] Kao-Peng Min,[2*] Yi-Jie Li,[3] Chi-Ting Ho,[4]
Walter Water,[5] and Cheng-Fu Yang[3,6**]

[1]Department of Aviation Communication and Electronics, Air Force Institute of Technology, Kaohsiung 820, Taiwan
[2]College of Engineering, National Formosa University, Huwei, Yunlin 632, Taiwan
[3]Department of Chemical and Materials Engineering, National University of Kaohsiung, Kaohsiung 811, Taiwan
[4]Department of Mechanical Design Engineering, National Formosa University, Yunlin 632, Taiwan
[5]Department of Electronic Engineering, National Formosa University, Yunlin 632, Taiwan
[6]Department of Aeronautical Engineering, Chaoyang University of Technology, Taichung 413, Taiwan

(Received September 3, 2025; accepted September 18, 2025)

Keywords: high-efficiency light absorber, visible light, antireflective layer, surface plasmon resonance

An absorber covering the visible to infrared spectrum can be utilized in various sensor applications. In this study, we designed and fabricated a multilayer absorber with the following structure from bottom to top: an iron substrate, followed by alternating layers of silicon dioxide (SiO_2) dielectric and metal layers in the order of iron (Fe), SiO_2, chromium (Cr), SiO_2, titanium (Ti), SiO_2, Ti again, and a top antireflective layer of magnesium fluoride (MgF_2). Through simulation and optimization, the absorber achieved an average absorptivity of 97.8% across a broad wavelength range from 350 to 2600 nm. Analysis revealed that this ultrabroadband and high absorption performance results from a combination of factors, namely, the antireflective effect of the MgF_2 layer on the top surface and the interplay of three distinct resonance mechanisms, which are Fabry–Perot resonance, propagating surface plasmon resonance, and localized surface plasmon resonance. These mechanisms work synergistically to enhance absorption across the target spectrum. Subsequently, the optimized absorber was deposited onto a silicon substrate by electron beam evaporation. The surface morphology and cross-sectional structure were examined by scanning electron microscopy, whereas the absorber's performance across the ultraviolet (UV), visible (Vis), and near-infrared (NIR) ranges was evaluated using a UV/Vis/NIR spectrophotometer.

1. Introduction

An optical absorber is a material or structure designed to efficiently absorb light at specific wavelengths. When incident light strikes the absorber, the optical energy is absorbed and converted into thermal energy or other forms of energy, rather than being reflected or

*Corresponding author: e-mail: D1481103@nfu.edu.tw
**Corresponding author: e-mail: cfyang@nuk.edu.tw
https://doi.org/10.18494/SAM5922

ISSN 0914-4935
https://myukk.org/

transmitted. Optical absorbers serve as core components in various sensing applications, with their sensing mechanisms typically based on several fundamental effects.[1,2]

1. Gas sensors: Certain gas-absorbing materials exhibit changes in their absorption spectra when specific gases are present, enabling the detection of gases such as NO_2, H_2S, and CO_2.[3] This spectral shift allows for the precise identification and quantification of target analytes.
2. Biosensors: Nano-optical absorbers, such as gold nanorods, can detect proteins, DNA, or cellular interactions. These sensors operate by monitoring changes in optical absorption characteristics caused by surface modifications when biomolecules bind to the absorber surface.
3. Temperature and heat flow sensors: Photothermal absorbing materials can accurately respond to temperature variations, making them ideal for noncontact thermal imaging and thermal radiation detection applications.
4. Optical imaging and microscopy: Optical absorbers find applications in high-sensitivity optical imaging systems and dark-field microscopy, where they enhance contrast and enable the detailed visualization of microscopic structures.[4,5]

Optical absorber sensors offer several compelling advantages.

1. High sensitivity: Capable of detecting minute environmental changes, including temperature fluctuations, gas concentration variations, and biomolecular binding events
2. Miniaturization compatibility: Suitable for integration into microchip platforms, including CMOS-compatible technologies, enabling compact sensor arrays
3. Noncontact operation: Ideal for remote monitoring and non-invasive measurement applications, eliminating the need for direct sample contact
4. Versatile applications: Adaptable to various sensing modalities across different fields, from environmental monitoring to biomedical diagnostics

Designing and fabricating an optical absorber with high absorptivity are key strategies for realizing a highly efficient sensor. High absorptivity ensures that incident light is effectively captured and converted, minimizing energy loss and maximizing the sensor's sensitivity and accuracy. This is particularly important in applications such as photodetectors, infrared sensors, and optical imaging systems, where performance strongly depends on the absorber's capability to efficiently interact with incoming light across specific wavelengths. Metamaterial absorbers are engineered structures composed of multiple layers of materials, primarily designed to enhance the absorption of electromagnetic radiation, such as light.[6–8] Unlike traditional absorbers, these advanced materials can be tailored at the subwavelength scale to exhibit unique electromagnetic properties not found in nature. Recent advancements in materials science and nanofabrication techniques have enabled the development of metamaterials with diverse multilayer configurations. By strategically varying the stacking order and material composition, researchers can precisely control absorption characteristics across a wide range of wavelengths. Compared with conventional absorbers, metamaterial absorbers offer several distinct advantages, including significantly enhanced absorption efficiency, broader tunability across different spectral regions, and greater potential for device miniaturization. These features make them highly attractive for a wide array of applications, such as sensors, stealth technology, thermal photovoltaics, and optical communication systems.

With the advancement of computer technology, numerous software tools have been developed for numerical simulation and analysis. Among these, the finite element method (FEM) has emerged in recent years as one of the most important tools in both academia and industry for understanding the design and working mechanisms of absorbers. By using FEM-based simulation software, researchers can analyze the performance of absorbers under various conditions. This allows users to adjust key parameters of the materials used—such as wavelength, thickness, and refractive index—to investigate how these variables affect the absorber's optical characteristics. Through such simulations, it becomes possible to predict absorption efficiency under different configurations and to determine the optimal design parameters, including thickness and absorption rate. In addition to theoretical analysis, we can integrate the simulation-based design to gain a clearer understanding of the absorber's expected performance prior to fabrication. This approach not only enables early-stage performance evaluation but also significantly reduces the time and cost associated with physical experiments and material usage. Finally, the designed optical absorber is fabricated using thermal evaporation, and its optical properties are experimentally measured. The resulting spectrum is then compared with the simulation data to validate the feasibility and accuracy of the design.

2. Methodology

The overall structure of the absorber is illustrated in Fig. 1(a), which shows the multilayer planar thin-film composition, and its cross-sectional view is shown in Fig. 1(b). The absorber designed in this study features a fully planar structure. Preliminary analysis results indicate that each layer extends laterally to a width of 300 nm, aligning with the periodicity of the unit cell. Initially, the thickness of each layer from bottom to top was set as follows: Fe substrate (h1, 100 nm), SiO_2 (h2, 80 nm), Fe (h3, 5 nm), SiO_2 (h4, 80 nm), Cr (h5, 5 nm), SiO_2 (h6, 100 nm), Ti (h7, 3 nm), SiO_2 (h8, 100 nm), Ti (h9, 3 nm), and a MgF_2 antireflective layer (h10, 80 nm). COMSOL software was then used for optimization simulations to determine the optimal thickness for each layer. In this experiment, a 4-inch p-type silicon wafer was used as the substrate.

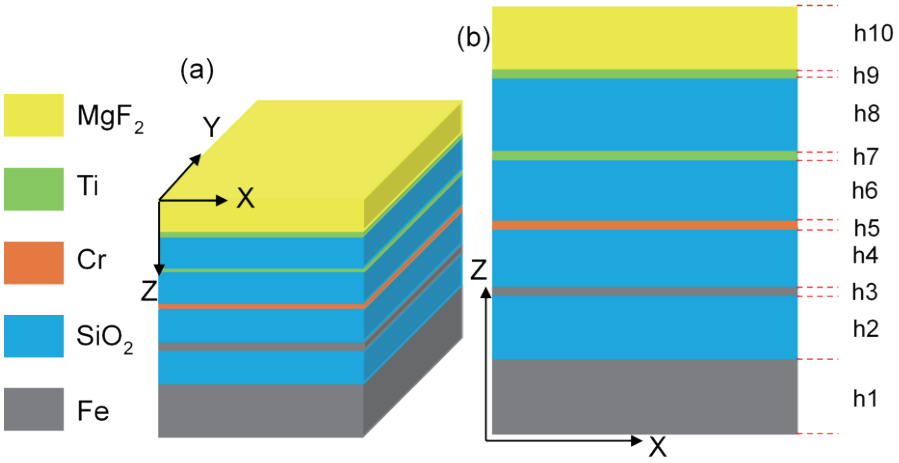

Fig. 1. (Color online) (a) Overall structure of the absorber and (b) its cross-sectional view.

The substrate was sequentially cleaned in acetone, methanol, and deionized water for 5 min each using an ultrasonic cleaner. These cleaning steps were carried out to remove surface grease and organic contaminants (acetone), eliminate residual acetone (methanol), and rinse off any remaining organic solvents (deionized water). Thin films were subsequently fabricated using an electron beam evaporation system. The vacuum chamber was evacuated to achieve a high vacuum state of 7.5×10^{-6} Torr. The deposition parameters were configured with specific thickness targets and deposition rates for each material: Fe at 0.5 Å/s, SiO_2 at 5 Å/s, Cr at 0.5 Å/s, Ti at 0.5 Å/s, and MgF_2 at 1 Å/s. The power settings and timing parameters for melting the target materials were established accordingly. Once the power supply was activated, the electron beam evaporation process commenced. Throughout the deposition process, quartz crystal oscillators installed within the chamber continuously monitored and measured both the thickness and deposition rate of the thin films being deposited. The surface morphology and cross-sectional structure of the topmost layer were examined by field-emission scanning electron microscopy (FE-SEM). For the comprehensive optical characterization of the thin films, optical measurements were performed using a HITACHI U4100 ultraviolet (UV)/visible (Vis)/near-infrared (NIR) spectrophotometer. The absorption characteristics were analyzed across a wavelength spectrum ranging from 300 to 2600 nm, a range specifically selected to capture the critical absorption behaviors relevant to thin film applications. This analytical approach provided detailed insights into the optical properties of the deposited films, enabling a thorough evaluation of their performance characteristics. The integration of these sophisticated measurement techniques facilitated a complete understanding of both the physical and optical attributes of the thin films, thereby enhancing the overall research outcomes and contributing meaningful data to the field of thin-film technology.

3. Simulation Results and Discussion

Figure 2 shows the simulated absorption spectrum obtained using COMSOL Multiphysics. The analyzed wavelength range spans from 300 to 3000 nm, with a step size of 10 nm per scan. According to the simulation results, the absorber exhibits an average absorptivity of 96.8% within the 350 to 2600 nm range, indicating excellent broadband absorption performance across the Vis and NIR regions. Owing to the initially high absorptivity values predicted by COMSOL simulation, this study places particular emphasis on comparing the simulation results before and after optimization. By doing so, we aim to verify whether the optimization process yields a significant improvement and to assess the practical feasibility of achieving such high absorption levels in actual fabrication. This comparison also helps identify potential discrepancies between simulation and experimental data, which may arise from factors such as material imperfections, fabrication tolerances, or deviations in layer thickness during deposition.

The initial optimization focused on the h2 SiO_2 layer. Although the results are not shown here, simulations revealed that increasing the thickness of the h2 SiO_2 layer from 50 to 150 nm produced only minor differences in the absorption spectrum compared with the original 80 nm design. Therefore, the thickness of the h2 SiO_2 layer was kept at 80 nm without further adjustment. Next, we analyzed the impact of the Fe layer in the h3 position. As shown in Fig.

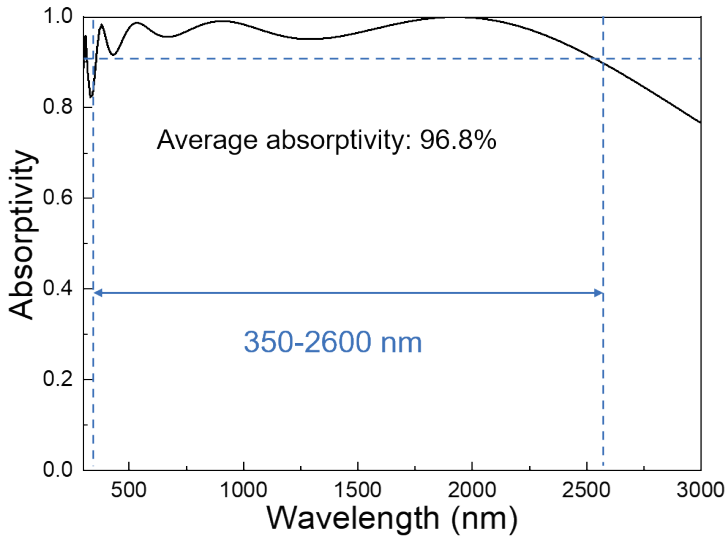

Fig. 2. (Color online) Absorption spectrum of the investigated absorber.

3(a), the absorption spectra for Fe thin films with thicknesses ranging from 10 to 50 nm were simulated. A notable trend was observed at the shorter wavelength of 300 nm, where the absorptivity increased with the Fe thin film thickness. This indicates that a thicker Fe layer enhances light–matter interactions in the UV to Vis range, thereby improving absorption. The results in Fig. 3(a) also revealed that increasing the Fe layer thickness from the initially set 5 to 8 nm resulted in a significant improvement in absorptivity. This improvement is further validated in Fig. 3(b), which compares the absorption spectra of Fe films with thicknesses of 5 and 8 nm. In the wavelength range below 700 nm, the Fe film with an 8 nm thickness consistently exhibited a higher absorptivity than that with a 5 nm thickness. These results clearly demonstrated that increasing the h3 Fe layer thickness enhances short-wavelength absorption performance, which is particularly important for achieving efficient broadband absorption. As shown in Fig. 3(b), the average absorptivity of the absorber with an 8-nm-thick Fe layer across the 350–2600 nm wavelength range reaches 97.0%, compared with 96.8% for the original 5 nm design, a 0.2% improvement. Although the increase may appear modest, it reflects a more optimized interaction of the absorption layers with incident light, especially in the UV to Vis range. Thus, fine-tuning the thickness of the h3 Fe layer plays a key role in tailoring the spectral response and enhancing the overall absorber efficiency.

Next, we analyzed the impact of the SiO_2 layer at the h4 position on the overall absorption rate. As shown in Fig. 4(a), we observed the simulated absorption spectra of SiO_2 films with thicknesses ranging from 50 to 150 nm. As the thickness of the SiO_2 layer increased, the absorption at longer wavelengths below the cut-off value of 0.9 exhibited a notable redshift. This redshift indicates an expansion in the effective absorption bandwidth. Furthermore, there was a significant increase in absorption in the UV region at around 350 nm, where the absorption surpassed 0.9. This trend is further emphasized in Fig. 4(b). Additionally, we examined the effect of SiO_2 layers at the h6 and h8 positions on the overall absorption rate. The results indicate that when the thicknesses of the SiO_2 layers at h6 and h8 were increased from 50 to 150 nm, the

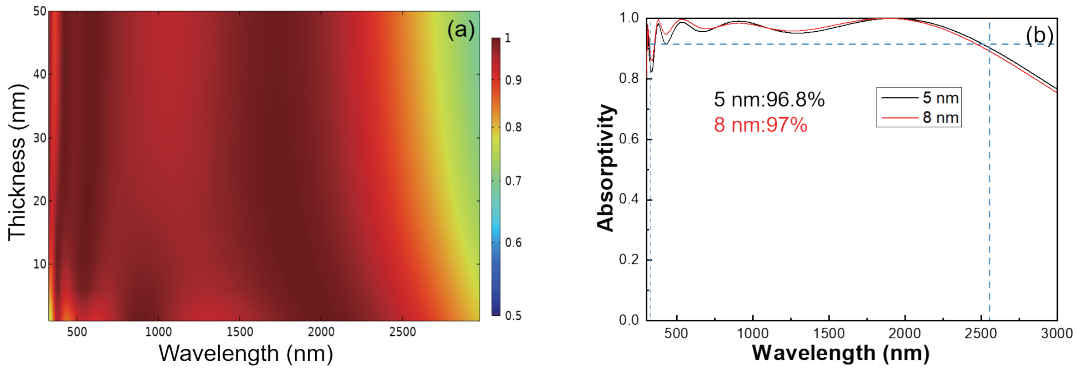

Fig. 3. (Color online) Effect of the thickness of h3 Fe layer on the (a) absorptivity distribution and (b) absorption spectra of the investigated absorbers.

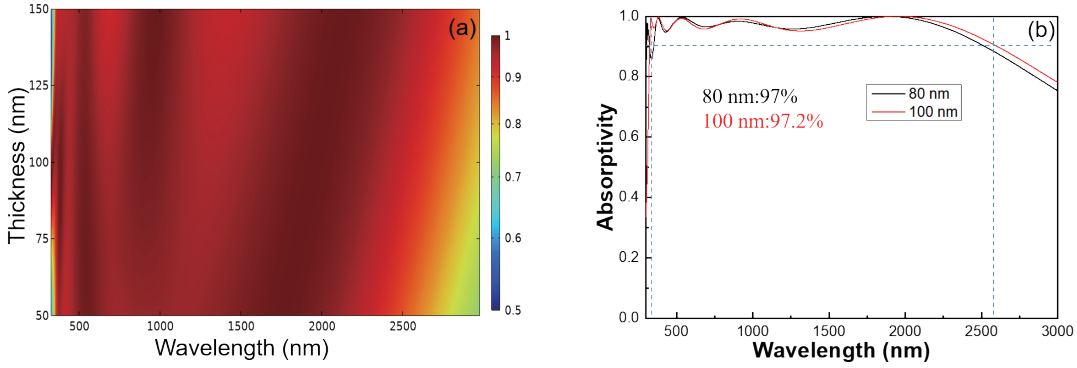

Fig. 4. (Color online) Effect of the thickness of h4 SiO_2 layer on the (a) absorptivity distribution and (b) absorption spectra of the investigated absorbers.

changes in the absorption spectra were almost identical to those observed for the h4 SiO_2 layer (results not shown here). However, similar to the h4 position, when the thickness exceeded 100 nm, the absorption in the UV region began to decrease. Compared with the initial design of 80 nm, a SiO_2 layer thickness of 100 nm at the h4 position yielded improved absorption performance. Similarly, the absorption spectra for the h6 and h8 SiO_2 layers show similar trends, with the optimal performance occurring at a thickness of approximately 100 nm. According to the absorption spectrum shown in Fig. 4(b), a SiO_2 thickness of 100 nm results in an average absorption rate of 97.2% over the 350–2600 nm wavelength range, which is a 0.2% improvement over the original 97% absorption rate. The thicknesses of the SiO_2 layers at the h6 and h8 positions were also typically set at 100 nm, further confirming that the effects of different SiO_2 layer thicknesses on overall absorption are similar.

The observed redshift and bandwidth expansion with increasing SiO_2 thickness can be attributed to enhanced optical interference effects, which help improve light confinement and extend the absorption range into the infrared region. The increase in UV absorption at around 350 nm suggests that a thicker SiO_2 layer is effective in optimizing the coupling of light at this wavelength, likely because of a more favorable optical path length or enhanced resonant modes

within the film. However, when the thickness exceeds 100 nm, the absorption in the UV region begins to decline, which can be explained by the increasing thickness leading to increased reflection losses or phase mismatches that disrupt constructive interference at shorter wavelengths. The fact that the behaviors of SiO_2 layers at h4, h6, and h8 positions are similar suggests that the position of the SiO_2 layer within the structure does not significantly affect the overall absorption characteristics, as long as the layer thickness is optimized. This result provides flexibility in the design process, as it demonstrates that the SiO_2 layer thickness can be controlled independently of the specific position within the stack. Overall, a thickness of 100 nm for the SiO_2 layer appears to strike an optimal balance for maximizing broadband absorption. This thickness ensures good absorption performance in both the UV and infrared regions without significant trade-offs. For future work, further optimization could include exploring the use of graded-index SiO_2 or multilayer designs to refine the spectral response across different regions without sacrificing absorption efficiency.

The analysis result of the h5 Cr layer is shown in Fig. 5(a). From this figure, we can observe the simulated absorption rates of Cr thin films with thicknesses ranging from 1 to 50 nm. Compared with the initial setting of 5 nm, there is no significant difference in absorption performance across the thickness range. As a result, the original parameter of 5 nm was maintained without any adjustments. The data from the h5 Cr layer analysis suggests that varying the thickness of the Cr film within the range of 1 to 50 nm does not lead to any considerable changes in absorption rate. This behavior indicates that, for this particular material and configuration, the 5 nm thickness is already optimized in terms of absorption performance. Given the lack of significant improvement by altering the thickness, there is no need to adjust the original 5 nm setting. This finding highlights an important aspect of material and design optimization, i.e., not all layers require the fine-tuning of thickness to achieve optimal performance. In this case, the Cr layer appears to reach a performance plateau in terms of absorption once the thickness is set at 5 nm.

The analysis result of the h7 Ti layer is presented in Fig. 5(b). In this figure, the simulated absorption rate of Ti thin films with thicknesses ranging from 1 to 50 nm is shown. Compared

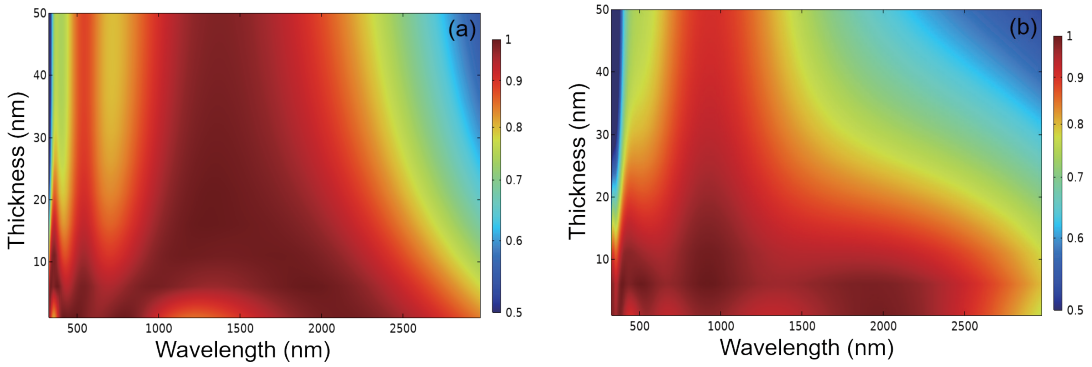

Fig. 5. (Color online) Effects of the thicknesses of (a) h5 Cr and (b) h7 Ti layers on the absorptivity distribution of the investigated absorbers.

with the initial setting of 3 nm, the absorption rate improves as the thickness reaches 5 nm. According to the absorption spectrum results (not shown here), the average absorption rate of the 5-nm-thick Ti layer across the 350–2600 nm range is 97.5%, which represents a 0.3% increase from the previously analyzed 97.2% absorption rate. On the other hand, the analysis result of the h9 Ti layer is shown in Fig. 6(a). Similar to the h7 analysis result, the analysis result of the h9 Ti layer (not shown here) presents the simulated absorption rate of Ti thin films with thicknesses ranging from 1 to 50 nm. Compared with the initial 3 nm thickness, the highest absorption rate is observed at 2 nm. According to the absorption spectrum shown in Fig. 6(b), the average absorption rate of the 2-nm-thick Ti layer in the 350–2600 nm range is 97.6%, which is a 0.1% increase over the original 97.5% absorption rate. The results from both the h7 and h9 Ti layer analyses demonstrate the relationship between film thickness and absorption rate.

In the case of the h7 Ti layer, a thicker film (5 nm) showed a notable improvement in absorption rate compared with the initial 3 nm setting. This suggests that, for this specific configuration, a slight increase in film thickness enhances the material's capability to absorb light, especially across a wide wavelength range (350–2600 nm). For the h9 Ti layer, a thinner film (2 nm) provided a marginally higher absorption rate than the 3 nm baseline. Although the increase was smaller (0.1%), it still indicates that thinner Ti films may be preferable for certain applications where a slight enhancement in absorption is critical. These findings raise important questions for future optimization, such as the following: Could further adjustments in thickness yield additional improvements in absorption performance? Are the observed trends consistent across different materials, or are they unique to Ti films in this particular thickness range? Additionally, the minor differences in absorption rate between the h7 and h9 configurations highlight the sensitivity of material performance to film thickness, suggesting that the fine-tuning of these parameters could be key in achieving optimal optical characteristics for specific-use cases.

The analysis reuslt of the h10 MgF_2 antireflective layer's impact on the overall absorption rate is presented in Fig. 7(a). In this figure, the simulated absorption rates of MgF_2 thin films with thicknesses ranging from 50 to 150 nm are shown. Compared with the initial setting of 80

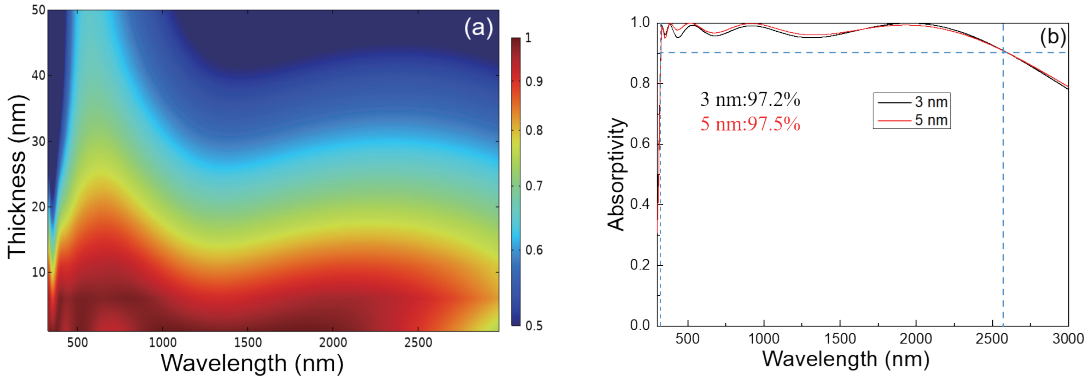

Fig. 6. (Color online) Effect of the thickness of h9 Ti layer on the (a) absorptivity distribution and (b) absorption spectra of the investigated absorbers.

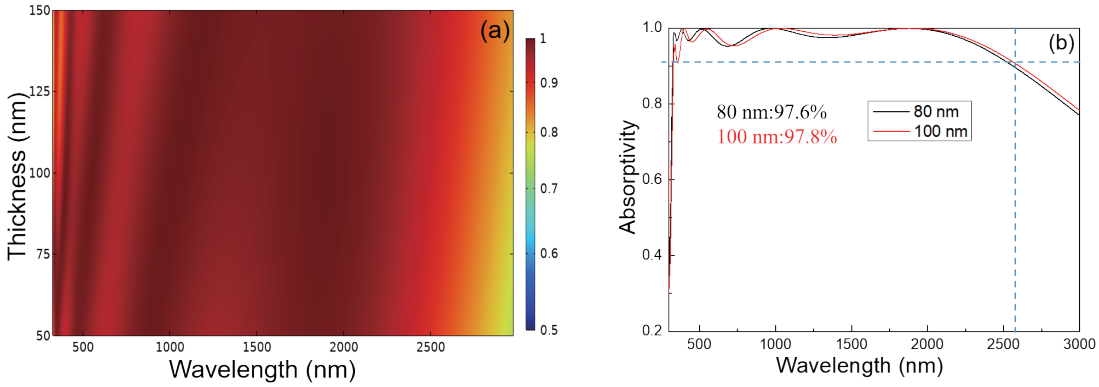

Fig. 7. (Color online) Effect of the thickness of h10 MgF_2 layer on the (a) absorptivity distribution and (b) absorption spectra of the investigated absorbers.

nm, the absorption rate was improved when the thickness was increased to 100 nm. According to the absorption spectrum shown in Fig. 7(b), average absorption rate of the 100-nm-thick MgF_2 layer over the 350–2600 nm range is 97.8%, which represents a 0.2% increase compared with the original absorption rate of 97.6%. The results indicate that the thickness of the MgF_2 antireflective layer plays a significant role in improving the absorption characteristics of the structure. Specifically, the 100-nm-thick MgF_2 layer achieves the highest absorption rate in the tested range, with a 0.2% increase in average absorption rate over the baseline of 97.6%. This suggests that optimizing the thickness of the antireflective layer can have a direct impact on the overall optical performance, particularly in enhancing light absorption over a wide spectral range. This behavior is consistent with the general principle that the antireflective layer not only reduces reflection losses but also improves the total absorption by improving the coupling of light into the underlying layers. The 100 nm thickness appears to be a favorable choice for this material system, balancing the trade-off between increasing thickness and diminishing returns in absorption performance. Further increases in thickness beyond 100 nm may lead to diminishing gains or even potential absorption losses due to additional scattering or interference effects within the film.

We optimized structural parameters by electron beam evaporation. Surface morphology observations reveal that the top layer of MgF_2 indicates a smooth and dense surface for the multilayer thin film structure prepared by this method (not shown here). Figure 8(a) displays the cross-sectional morphology of the multilayer thin film. From the results of cross-sectional structure analysis, the actual thicknesses of the layers were measured to be as follows: h1 = 190 nm, h2 = 83.7 nm, h3 = 14.0 nm, h4 = 86.5 nm, h5 = 9.77 nm, h6 = 83.7 nm, h7 = 9.37 nm, h8 = 82.3 nm, h9 = 10.2 nm, and h10 = 168.5 nm. In this study, the fabricated absorber achieved an average absorptivity of 90.3% across the 350–2600 nm wavelength range, as shown in Fig. 8(b). This value is slightly lower than that predicted by simulation, which showed a higher absorption rate. It is speculated that this difference arises owing to the variation in actual deposited layer thickness compared with the thickness used in the simulation. In

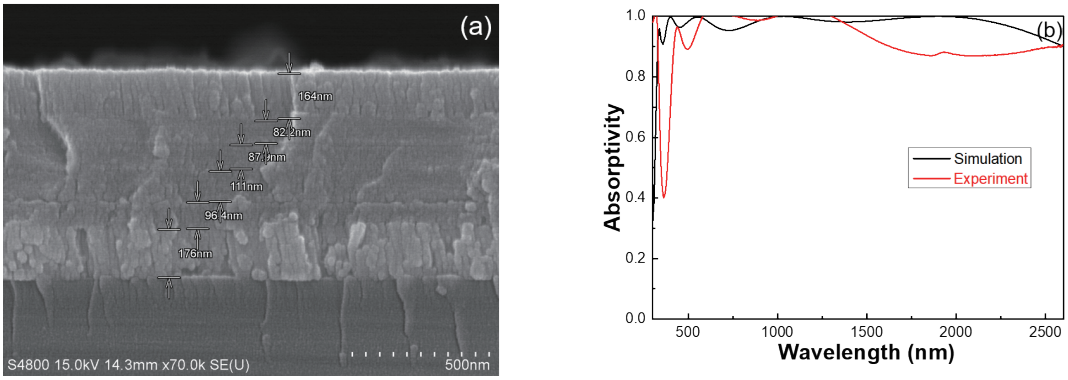

Fig. 8. (Color online) (a) Cross section of the fabricated absorber and (b) the comparison of absorption spectra of the simulated and fabricated absorbers.

simulations, precise layer thicknesses and material properties are critical for predicting the optical performance accurately. Even small deviations in thickness during the fabrication process can significantly impact the absorber's performance, particularly in such a broad wavelength range.

To further validate the model, we performed additional simulations using COMSOL using the actual deposited layer thicknesses. The results showed an average absorptivity of approximately 90%, which was very close to the measured experimental absorptivity. Moreover, the absorption trend across the wavelength range also showed a strong correlation with the experimental data, demonstrating that the simulation effectively captured the key optical behaviors of the absorber. This comparison between experimental and simulated data not only confirmed the feasibility of the simulation model but also highlighted the importance of precise fabrication techniques. Although small discrepancies between simulation and experimental results are expected, the close agreement in both absorptivity and trend supports the reliability of the model in predicting absorber performance under real-world conditions. This finding suggests that, with the careful control of fabrication parameters, the design can achieve optimized performance in practical applications, validating the model's usefulness for future absorber development.

4. Conclusions

In this study, the simulation results indicated that the optimal thicknesses for all the layers were h1 = 100 nm, h2 = 80 nm, h3 = 8 nm, h4 = 100 nm, h5 = 5 nm, h6 = 100 nm, h7 = 5 nm, h8 = 100 nm, h9 = 2 nm, and h10 = 100 nm. However, the actual fabricated layer thicknesses were h1 = 190 nm, h2 = 83.7 nm, h3 = 14.0 nm, h4 = 86.5 nm, h5 = 9.77 nm, h6 = 83.7 nm, h7 = 9.37 nm, h8 = 82.3 nm, h9 = 10.2 nm, and h10 = 168.5 nm. Clearly, there is a discrepancy between the simulated and actual values. The fabricated absorber in this study demonstrated an average absorptivity of 90.3% over the 350–2600 nm wavelength range, which is lower than the simulation result. This discrepancy is likely due to differences between the actual deposited

layer thicknesses and those used in the simulation. Finally, we used COMSOL to simulate the absorber with the actual deposited layer thicknesses. The results showed an average absorptivity of 90% across the 350–2600 nm wavelength range, closely matching the experimental measurements both in value and absorption trend. This confirms the reliability and feasibility of the simulation model.

Acknowledgments

This work was supported by Summit-Tech Resource Corp. and by projects under Nos. NSTC 113-2221-E-390-011 and NSTC 113-2221-E-005-042, and the funding of the Ministry of National Defense of the Taiwan under the 2025 Military Instructor Research Grant. We would like to thank Pitotech Co., Ltd. for teaching us the use of COMSOL Multiphysics® software.

References

1 H. Ma, K. Song, L. Zhou, and X. Zhao: Sensors **15** (2015) 7454.
2 X. Liu, K. Li, Z. Meng, Z. Zhang, and Z. Wei: Front. Phys. **9** (2021) 637602.
3 Y. E. Monfared and M. Qasymeh: Results Phys. **23** (2021) 103986.
4 M. Pan, Z. Su, Z. Yu, P. Wu, H. Jile, Z. Yi, and Z. Chen: Results Phys. **19** (2020) 103415.
5 M. L. Hakim, A. Hanif, T. Alam, M. T. Islam, H. Arshad, M. S. Soliman, S. M. Albadran, and Md. S. Islam: Nanomaterials **12** (2022) 2849.
6 G. Peng, P. X. Ke, L. C. Tseng, C. F. Yang, and H. C. Chen: Photonics **10** (2023) 804.
7 S. Anwar, Q. Khan, G. Ali, M. Khan, and M. Maqbool: Eur. Phys. J. D **77** (2023) 69.
8 Y. Du, C. H. Wang, P. X. Ke, C. F. Yang, and J. J. Lin: Int. J. Modern Phys. B **39** (2025) 2540022.